Monthly Notices
of the
ROYAL ASTRONOMICAL SOCIETY

MNRAS **467,** 155–163 (2017)
Advance Access publication 2017 January 11

doi:10.1093/mnras/stx044

# 325 and 610 MHz radio counterparts of SNR G353.6−0.7 also known as HESS J1731−347

Nayana A. J.,[1⋆] Poonam Chandra,[1⋆] Subhashis Roy,[1⋆] David A. Green,[2] Fabio Acero,[3] Marianne Lemoine-Goumard,[4] Alexandre Marcowith,[5] Alak K. Ray[6] and Matthieu Renaud[5]

[1]*National centre for Radio Astrophysics, Tata Institute of Fundamental Research, PO Box 3, Pune 411 007, India*
[2]*Astrophysics Group, Cavendish Laboratory, 19 J. J. Thomson Avenue, Cambridge CB3 0HE, UK*
[3]*Laboratoire AIM, IRFU/SAp – CEA/DRF – CNRS – Université Paris Diderot, Bat. 709, CEA-Saclay, F-91191 Gif-sur-Yvette Cedex, France*
[4]*Centre d'Etudes Nucléaires de Bordeaux Gradignan, Université Bordeaux, CNRS/IN2P3, F-33175 Gradignan, France*
[5]*Laboratoire Univers et Particules de Montpellier (LUPM), Université de Montpellier, CNRS/IN2P3, F-34095 Montpellier, France*
[6]*Tata Institute of Fundamental Research, Homi Bhabha Road, Mumbai 400001, India*

Accepted 2017 January 6. Received 2016 December 13; in original form 2016 October 20

## ABSTRACT

HESS J1731−347 also known as SNR G353.6−0.7 is one of the five known shell-type supernova remnants (SNRs) emitting in the very high energy (VHE, energy > 0.1 TeV) $\gamma$-ray domain. We observed this TeV SNR with the Giant Metrewave Radio Telescope (GMRT) in 1390, 610 and 325 MHz bands. In this paper, we report the discovery of 325 and 610 MHz radio counterparts of the SNR HESS J1731−347 with the GMRT. Various filaments of the SNR are clearly seen in the 325 and 610 MHz bands. However, the faintest feature in the radio bands corresponds to the peak in VHE emission. We explain this anti-correlation in terms of a possible leptonic origin of the observed VHE $\gamma$-ray emission. We determine the spectral indices of the bright individual filaments, which were detected in both the 610 and the 325 MHz bands. Our values range from −1.11 to −0.15, consistent with the non-thermal radio emission. We also report a possible radio counterpart of a nearby TeV source HESS J1729−345 from the 843 MHz Molonglo Galactic Plane Survey and the 1.4 GHz Southern Galactic Plane Survey maps. The positive radio spectral index of this possible counterpart suggests a thermal origin of the radio emission of this nearby TeV source.

**Key words:** acceleration of particles – radiation mechanisms: non-thermal – cosmic rays – ISM: individual objects: SNR G353.6−0.7 – ISM: supernova remnants – radio continuum: ISM.

## 1 INTRODUCTION

Galactic cosmic rays are energetic particles believed to be mostly composed of hadrons with energies ranging from ∼0.1 to $10^{8-9}$ GeV (Blandford & Eichler 1987). How are these particles accelerated to these high energies remains a fundamental question. Supernova remnant (SNR) shocks are considered as one of the probable candidates of these particle acceleration sites (Blasi 2013). Cherenkov telescopes such as the High Energy Stereoscopic System (HESS), the Major Atmospheric Gamma Imaging Cherenkov Telescope and the Very Energetic Radiation Imaging Telescope Array System have discovered many very high energy (VHE; Energy > 100 GeV) $\gamma$-ray sources from the Galactic plane in the last decade (Degrange & Fontaine 2015). Association of spatially resolved shell-like $\gamma$-ray sources with SNRs is the signature of particle acceleration at supernova shocks.

Studying these objects provides a unique opportunity to probe the cosmic ray particles that emit high-energy $\gamma$-rays. However, so far, there are only five spatially resolved shell-like VHE sources firmly identified as SNRs (for a review, see Acero et al. 2015). These are RX J1713.7−3946 (Aharonian et al. 2004; H. E. S. S. Collaboration et al. 2016a), RX J0852.0−4622 (Aharonian et al. 2007; H. E. S. S. Collaboration et al. 2016b), RCW 86 (Aharonian et al. 2009; H. E. S. S. Collaboration et al. 2016c), SN 1006 (Acero et al. 2010) and HESS J1731−347 (Abramowski et al. 2011).

HESS J1731−347 was discovered (Aharonian et al. 2008) as a VHE $\gamma$-ray source in the HESS Galactic Plane Survey at $\alpha_{J2000} = 17^{h}31^{m}55^{s}$, $\delta_{J2000} = -34^{\circ}42'36''$ with no identified counterpart in other wavebands. Later, Tian et al. (2008) discovered a faint shell-type radio source SNR G353.6−0.7 with an angular size

⋆ E-mail: nayana@ncra.tifr.res.in (NAJ); poonam@ncra.tifr.res.in (PC); roy@ncra.tifr.res.in (SR)

**Table 1.** Details of GMRT observations.

| Frequency (MHz) | Date of observation (UT) | Time on source (h) | FWHM of primary beam (arcmin) | Number of pointings | Pointing centre RA (J2000) Dec. (J2000) |
|---|---|---|---|---|---|
| 325 | 2013 October 19.3 | 5.4 | 85.2 | 1 | $17^h31^m54.9^s$ $-34°42'36.00''$ |
| 610 | 2015 August 29.5 | 3.5 | 43 | 1 | $17^h32^m19.6^s$ $-34°43'30.00''$ |
| 1390[a] | 2013 December 19.1, 20.1 | 2.5 | 26.2 | 4 | $17^h32^m11.9^s$ $-34°37'60.00''$ |
| | | | | | $17^h32^m29.9^s$ $-34°49'60.00''$ |
| | | | | | $17^h31^m35.9^s$ $-34°44'60.00''$ |
| | | | | | $17^h29^m35.9^s$ $-34°32'60.00''$ |

[a]In the 1390 MHz band, observations were taken in two consecutive days with four pointings to cover SNR G353.6−0.7 and HESS J1729−345.

of ≈ 30 arcmin, in spatial coincidence with HESS J1731−347 in the Southern Galactic Plane Survey (SGPS) at 1420 MHz (Haverkorn et al. 2006) and Molonglo Galactic Plane Survey (MOST) at 843 MHz (Green et al. 1999). Tian et al. (2008) derived an integrated flux density of 2.2±0.9 Jy at 1420 MHz by azimuthally averaging the radio intensity in rings about the centre of the SNR. Later, a deeper $\gamma$-ray observation of HESS J1731−347 revealed the shell-like morphology in $\gamma$-rays as well (Abramowski et al. 2011), which made HESS J1731−347 the fifth member of the VHE shell SNR group. HESS J1731−347 was also observed with the *Fermi* Large Area Telescope, but no GeV counterpart was detected (Yang et al. 2014). HESS J1731−347 was detected in X-rays in archival *ROSAT* data (Aharonian et al. 2008; Tian et al. 2008). The X-ray emission was found to be non-thermal (Tian et al. 2010; Abramowski et al. 2011; Bamba et al. 2012), indicating that the electron population producing these non-thermal X-rays are of TeV energies. A compact object XMMU J173203.3−344518 was detected at the centre of the remnant by Halpern & Gotthelf (2010a) using *XMM–Newton* archival data. This object was considered as a central compact object (CCO) associated with SNR G353.6−0.7 (Acero et al. 2009; Halpern & Gotthelf 2010a; Tian et al. 2010). Tian et al. (2008) estimated the distance to the SNR as 3.2±0.8 kpc, by assuming the nearby H II region G353.42−0.37 to be at the same distance as the SNR.

In this paper, we present the Giant Metrewave Radio Telescope (GMRT; Swarup et al. 1991) observations of SNR G353.6−0.7 in the 325, 610 and 1390 MHz bands. Our detections in the 325 and 610 MHz bands are the lowest frequency detections of the SNR thus far. We compare the shell morphology of the SNR from our low-frequency measurements with those of other published high-frequency results. We also measure the spectral index of different filaments of the SNR. The paper is organized as follows: in Section 2, we explain the GMRT observations and in Section 3, we briefly discuss the method of data analysis. Section 4 contains the results and discussions and the Section 5 contains the summary and conclusions.

## 2 GMRT OBSERVATIONS

We observed SNR G353.6−0.7 with the GMRT at 325, 610 and 1390 MHz. The 325, 610 and 1390 MHz observations were carried out on 2013 October 19.3 (UT), 2015 August 29.5 (UT) and 2013 December 19.1,20.1 (UT), respectively. In the 325 and 610 MHz bands, the GMRT full width at half-maximum (FWHM) of primary beam is 85.2 and 43 arcmin, respectively, and only one pointing was necessary to cover the SNR. In the 1390 MHz band, the FWHM is 26.2 arcmin, and observations were taken in four pointings since the field of view is less than the source extent. Three pontings were done towards the SNR region and one pointing towards another TeV source HESS J1729−345, just 30 arcmin away from the SNR (Aharonian et al. 2008). The 1390 MHz observations were carried out on two consecutive days so as to increase the sensitivity. Details of the GMRT observations are given in Table 1.

The data were recorded with an integration time of 16.1 s. For all the frequency bands, the bandwidth chosen was 33 MHz split into 256 frequency channels. All the observations were taken with Automatic Level Control (ALC) on. The ALC controls the amplitude gains of the antennas with a negative feedback loop at the output of each antenna. It ensures a safe operating point without running the electronics into saturation. 3C286 was used as the flux density calibrator at all frequencies. At 325 MHz, sources J1714−252 and J1830−360 were used as the phase calibrators. J1830−360 and J1714−252 were used as phase calibrators at the 610 and 1390 MHz observations, respectively. The flux density calibrator was used to calibrate antenna gains, and the phase calibrators were used to correct for phase variations due to atmospheric fluctuations. The phase calibrators were also used for bandpass calibration.

The system temperature ($T_{sys}$) correction was implemented by determining the self-powers of each antenna with ALC off in a separate test observation run, taken in 2015 December in the 325, 610 and 1390 MHz bands. The SNR and the flux calibrator were observed for 10 min each. Power equalization was done on the SNR. Antenna self-powers (total power measured by antenna) were recorded for all antennas, for each time stamp (16.1 s) and for all channels.

## 3 DATA ANALYSIS

### 3.1 Calibration and imaging

The data were analysed using Astronomical Image Processing System (AIPS) developed by the National Radio Astronomy Observatory (NRAO; Greisen 2003). One antenna was not working in the 325 as well as 610 MHz band observations, whereas three antennas were not working in the 1390 MHz observations due to technical problems. These antennas were excluded from further analysis. Corrupted data due to instrumental problems were removed using standard AIPS routines. Channels with radio frequency interference (RFI) were flagged using the task SPFLG. [1] This task displays the *uv* data in a grid with frequency channels in the *x*-axis and time in

[1] Detailed documentation of SPFLG as well as all other AIPS tasks mentioned in this section is available at http://www.aips.nrao.edu/cook.html

the $y$-axis. It also provides interactive options to inspect and flag the data. Amplitude and phase calibration were done for single channel and the solutions were applied to all the channels in the data. Bandpass calibration was done using the phase calibrator. At 1390 MHz band, the two days of data were combined together after calibration using the AIPS task DBCON. The target source data were averaged in small frequency bins so as to reduce the effect of bandwidth smearing that reduces the amplitude of the visibility. The fractional reduction in the strength of a source at a radial distance $r$ from the centre of field to that at the centre of field is given by

$$R_{\rm b} = 1.064 \frac{\theta_{\rm b}\nu_0}{r\Delta\nu} {\rm erf}\left(0.833\frac{r\Delta\nu}{\theta_{\rm b}\nu_0}\right),$$

where $\theta_{\rm b}$ is the angular size of synthesized beam, $\nu_0$ is the centre of the observing band and $\Delta\nu$ is the bandwidth of the signal. We averaged a few channels in such a way that the fractional reduction in the strength of a source at the edge of the field is 5 per cent. For example, in the 325 MHz band, the adjacent four channels were averaged to obtain a channel width of 0.5 MHz and eight channels were averaged to get a channel width of 1 MHz in the 610 MHz band. In the 1390 MHz, 10 channels were averaged to obtain a channel width of 1.25 MHz. These sub-channels were stacked together while making images.

Multifacet imaging was done using the task IMAGR as the two-dimensional fast fourier transform leads to a flat sky approximation. Multifacet imaging takes care of the phase errors due to this approximation. The number of facets was calculated using the AIPS task SETFC. A total of 55 facets were created for the 325 MHz data, and 37 facets in the 610 MHz band. In the 1390 MHz band, 31 facets were created for each pointing. First, high-resolution images of the compact sources were made for self-calibration using visibilities from baselines greater than 1 km, i.e. excluding the GMRT central square antennas. The images were made using *uv* range 2–25, 3–30 and 5–105 k$\lambda$ in the 325, 610 and 1390 MHz bands, respectively. Only point sources were cleaned, whereas the SNR region and other extended sources were not cleaned during high-resolution imaging. A few rounds of phase only self-calibration and two rounds of amplitude and phase self-calibration were run. All the clean components were subtracted from the *uv* data using task UVSUB that takes the *uv* data set and clean component files as inputs and subtracts the clean components from the *uv* data set. This procedure was followed essentially to remove the compact sources in the field since the SNR has extended structure.

Finally, low-resolution maps were made using small *uv* range (only central square data). This corresponded to a *uv* range of 0–2, 0–3 and 0 to 5 k$\lambda$ for the 325, 610 and 1390 MHz bands data, respectively. The shortest baselines we have for these observations are $B_{\rm min} \sim 50$, 100 and 500$\lambda$ for the 325, 610 and 1390 MHz bands, respectively. In the 1390 MHz band, a significant fraction of short baselines was flagged due to RFI. This makes the interferometer sensitive to angular scales less than $0.6\lambda/B_{\rm min}$ (Basu et al. 2012), provided there are enough measurements at short baselines. All facets in each pointing were combined using task FLATN. This task does an interpolation of multiple fields produced by the task IMAGR into a single image. In the 1390 MHz band, the final map was made by combining maps of all three pointings towards the SNR. Finally, primary beam corrections were made for all the maps.

Our observations are sensitive up to the largest angular scales of $\sim$41.2, 20.6 and 4.0 arcmin in the 325, 610 and 1390 MHz bands, respectively. Since the size of the SNR G353.6−0.7 is 30 arcmin, we do not have enough short spacings to completely measure the flux density of SNR at the 610 and 1390 MHz frequencies. However, the effect of missing flux is small in the 325 MHz map. A simulation was done to quantify the flux density missing using AIPS task UVMOD. This task allows us to modify the *uv* data by adding a model. A sky model of a solid disc of 30 arcmin in diameter was simulated and then sampled to the GMRT *uv*-coverage at the 325 MHz. The *uv*-data were then imaged and more than 97 per cent of flux density was recovered. Thus, our GMRT 325 MHz map suffer from a maximum of 3 per cent missing flux while imaging a 30 arcmin structure. Simulations for missing flux were done for individual filaments at 610 MHz, which we describe in Section 4.3.

The SNR was detected in the 325 and 610 MHz bands (see Fig. 1); however, we do not detect it in the 1390 MHz band because of the missing flux due to lack of short spacings and the sensitivity limitation.

### 3.2 System temperature ($T_{\rm sys}$) correction

The SNR G353.6−0.7 is close to the Galactic plane, where the sky temperature ($T_{\rm sky}$) is high due to the contribution of the Galactic diffuse emission. Since observations were done with the ALC ON in its default mode and ALC controls the antenna gains automatically, the antenna gains are reduced with respect to the calibrators and the flux density measurements will be less than their true value. As the antenna self-powers are proportional to the system temperatures ($T_{\rm sys}$), a correction can be found by measuring the ratio of antenna self-powers towards the target source and flux calibrator, under the assumption that the contribution of electronics towards the system temperature will not change significantly between the days of observations at the same frequency. The actual flux density of the target source can be recovered by applying this $T_{\rm sys}$ correction.

Test observations for the $T_{\rm sys}$ correction were taken in 2015 December, and the data were analysed using GMRT specific offline packages. After removing corrupted data, the ratio of self-powers was found for each antenna. The mean and the rms of the ratios were computed to estimate the average $T_{\rm sys}$ correction. A detailed explanation of $T_{\rm sys}$ correction can be found in GMRT technical report by Roy (2006)[2].

Another way of obtaining $T_{\rm sys}$ correction is to estimate $T_{\rm sky}$ at both target source and flux calibrator positions from the all-sky temperature map. Haslam 408 MHz full sky temperature map by Haslam et al. (1982) and 150 MHz temperature measurements by Landecker & Wielebinski (1970) were used to obtain $T_{\rm sky}$ at both positions. The $T_{\rm sky}$ at 325, 610 and 1390 MHz were calculated by assuming a spectral index of −2.55 for Galactic diffuse emission (Roger et al. 1999). System temperature has contributions from the sky, ground and receiver. The ground temperature ($T_{\rm g}$) and receiver temperature ($T_{\rm rec}$) were taken from a GMRT technical report[3].

The $T_{\rm sys}$ correction obtained for each frequency from GMRT test observations, from the Haslam map (Haslam et al. 1982) and from the 150 MHz map (Landecker & Wielebinski 1970) are given in Table 2. The $T_{\rm sys}$ correction from the Haslam map is 54.6 per cent greater than that obtained from GMRT test observations at 325 MHz and 27.6 per cent greater at 610 MHz. The correction from the 150 MHz map is 39.7 per cent greater than that of the GMRT correction factor at 325 MHz and 17.0 per cent greater at 610 MHz. At 1390 MHz, all three correction factors are similar. A similar

[2] http://ncralib1.ncra.tifr.res.in:8080/jspui/handle/2301/315
[3] http://gmrt.ncra.tifr.res.in/gmrt_hpage/Users/doc/manual/Manual_2013/manual_20Sep2013.pdf

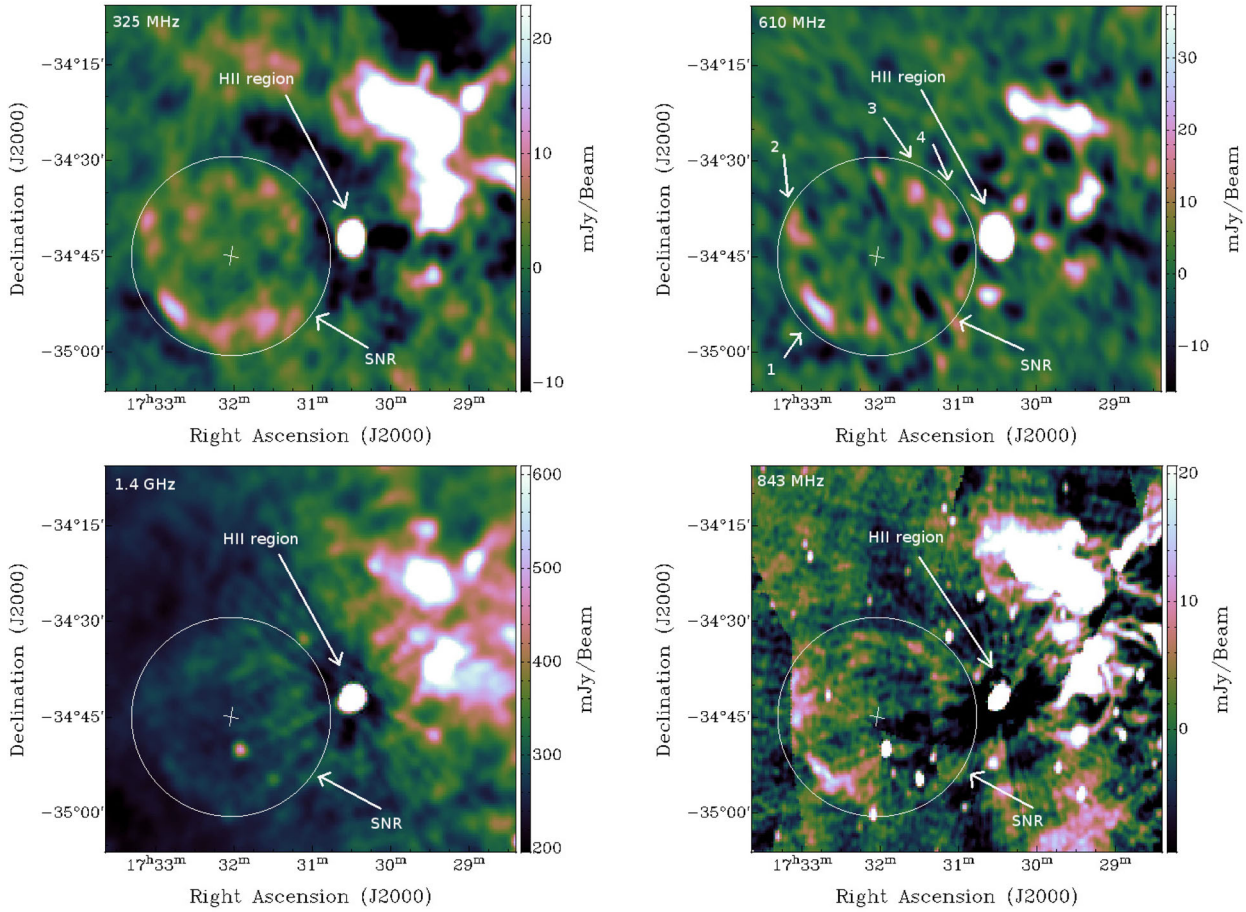


**Figure 1.** Top left: the GMRT low-resolution map of the field containing SNR G353.6−0.7 at 325 MHz. Map resolution is 135×97 arcsec$^2$, rms = 4.8 mJy beam$^{-1}$. Top right: we show GMRT low-resolution map of the field containing SNR G353.6−0.7 at 610 MHz. Map resolution is 150×105 arcsec$^2$, rms = 4 mJy beam$^{-1}$. Here the areas marked by 1, 2, 3, 4 are the filaments for which spectral indices were estimated. Compact sources have been removed from both 325 and 610 MHz GMRT maps. For comparison, we show the SGPS map (Haverkorn et al. 2006) of the field containing SNR G353.6−0.7 at 1420 MHz with resolution is 100×100 arcsec$^2$, rms = 10 mJy beam$^{-1}$ ( bottom left ), as well as the MOST map (Green et al. 1999) of the field containing SNR G353.6−0.7 at 843 MHz. with resolution is 49.71×43.00 arcsec$^2$, rms = 3 mJy beam$^{-1}$ ( bottom right). The circles in all four images are of same size and centred at the CCO position (marked with a cross) indicate the area enclosing SNR G353.6−0.7. The colour scheme used in the maps is cubehelix (Green 2011).

**Table 2.** $T_{sys}$ correction from different methods.

| Frequency (MHz) | Correction (GMRT) | Correction using 408 MHz map (Haslam et al. 1982) | Correction using 150 MHz map (Landecker & Wielebinski 1970) |
|---|---|---|---|
| 325 | 4.01±0.51 | 6.20 | 5.60 |
| 610 | 1.59±0.13 | 2.03 | 1.86 |
| 1390 | 1.08±0.04 | 1.10 | 1.10 |

*Notes*. Corection (GMRT) is the mean of ratios of antenna self-powers measured towards SNR and flux calibrator. The ¿ncertainties are at 1$\sigma$ level. Correction (Haslam et al. 1982) and correction (Landecker & Wielebinski, 1970) are corrections obtained from the sky temperature maps.

trend in $T_{sys}$ corrections with GMRT observations and the Haslam map was also reported by Marcote et al. (2015).

The $T_{sky}$ measurements using GMRT at 240 MHz was determined by Sirothia (2009). They report differences in the $T_{sky}$ measurements obtained from the Haslam map and GMRT measurements, and the rms of percentage differences is 56 per cent. This discrepancy might be due to the assumption of a constant spectral index of −2.55 across the whole sky, while determining $T_{sky}$ using the Haslam map. This assumption need not hold in all regions of the sky, especially towards the Galactic Centre where significant contribution from thermal emission is expected. Moreover, variation in $T_{rec}$ with elevation and ambient temperatures (Sirothia 2009) will also affect the $T_{sys}$ measurements. Estimation from the Haslam map does not account for these issues. Hence, $T_{sys}$ correction from GMRT test observation seems to be more reliable than the one obtained from the Haslam map. In this paper, we use the correction factor from GMRT observations to scale the observed flux density values.

**Table 3.** Physical dimensions of four filaments in angular units and flux densities at 325 and 610 MHz.

| Filament | Length (arcmin) | Width (arcmin) | $S_{\rm int}$ (325 MHz) (mJy) | $S_{\rm int}$ (610 MHz) (mJy) | Spectral index |
|---|---|---|---|---|---|
| Filament 1 | 11 | 3 | 106.22 | 68.67 | $-0.70 \pm 0.19$ |
| Filament 2 | 6 | 2.8 | 121.66 | 58.94 | $-1.11 \pm 0.22$ |
| Filament 3 | 5.4 | 3.7 | 56.90 | 41.55 | $-0.50 \pm 0.30$ |
| Filament 4 | 5.9 | 3.4 | 42.99 | 39.45 | $-0.15 \pm 0.32$ |

*Note*. $S_{\rm int}$ denotes the integrated flux density of the filaments at each frequencies.

### 3.3 Spectral analysis

Analysis of spectral index ($\alpha$, where the radio flux density $S_\nu$ at frequency $\nu$ is related to $\alpha$ as $S_\nu = \nu^\alpha$) provides information about the nature of the radio emission. Since the full shell structure was not detected in the 610 MHz band, we determined spectral indices for four filaments (see filaments marked 1, 2, 3 and 4 in the top right of Fig. 1 and Table 3) that were detected in both the 610 and 325 MHz bands. The sizes of the filaments are less than 11 arcmin and are well below the maximum angular scales that can be mapped with GMRT in both the 325 and 610 MHz bands. We estimated a missing flux of less than 2 per cent for these filaments in both the 325 and 610 MHz bands in our observations. Thus, these structures are not affected from significant missing flux problems.

To determine the spectral indices, both 325 and 610 MHz maps were convolved to the coarser resolution ($150\times105$ arcsec$^2$) using the AIPS task CONVL. Both maps were then aligned to same geometry using the AIPS task OHGEO. The flux density of the same region over both maps was determined using task BLSUM and rescaled with the $T_{\rm sys}$ correction factor to get the actual flux density. The total error $\sigma_{\rm total}$ in the flux density measurement is a combination of errors from calibration and rms noise of the map. Hence, the uncertainties in flux density measurements are estimated as

$$\sigma_{\rm total} = \sqrt{\sigma_{\rm rms}^2 + \sigma_{\rm cal}^2}, \quad (1)$$

where $\sigma_{\rm rms}$ is the map rms noise and $\sigma_{\rm cal}$ is the calibration error. We assumed that the calibration errors are 10 per cent of the measured flux density. The errors on spectral indices are computed using standard error propagation formulas.

## 4 RESULTS AND DISCUSSION

### 4.1 Morphology of SNR G353.5−0.7

Our observations with the GMRT have revealed the radio morphology of the SNR at the 325 and 610 MHz frequencies. Fig. 1 (top panels) clearly shows a shell-like structure with filaments. The extent of shell structure is $\sim 30$ arcmin, consistent with that measured by Tian et al. (2008) from the SGPS map at 1.4 GHz (bottom left panel of Fig. 1; Haverkorn et al. 2006). The 325 MHz map has an rms of 4.8 mJy beam$^{-1}$ with a resolution of $135\times97$ arcsec$^2$. Since the SNR is extended, low-resolution maps were made in order to get better signal-to-noise ratio per synthesized beam. The radio emission is brightest in the filament seen towards the south-east, and is detected at $10\sigma$ significance. The faintest filament is towards the north and is detected at $3\sigma$ significance. The rms of the 610 MHz map is 4 mJy beam$^{-1}$ for a resolution of $152\times105$ arcsec$^2$. The diffuse faint emission towards the north is not detected in the 610 MHz band. This is due to sensitivity limitation and poor sampling at short baselines. The smaller field of view at the 610 MHz (43 arcmin) also limits better mapping of the 30 arcmin structure in the sky. Filaments 1 and 2 (top right panel of Fig. 1) seen in the 610 MHz GMRT map are also seen in the MOST 843 MHz map (bottom right panel of Fig. 1; Green et al. 1999). The brightest emission comes from the south-east filament (Filament 1), which is also the case in the GMRT 325 MHz image.

The SNR is not detected in the 1390 MHz GMRT map. The map rms is 1.8 mJy beam$^{-1}$. The shortest baseline available with the GMRT at 1390 MHz is $\sim 500\lambda$. This makes the interferometer sensitive to a maximum angular scale of 4 arcmin. Thus, it is not possible to image the full SNR shell at 1390 MHz using the GMRT. But the bright filamentary structures of small angular size can be detected. However, we did not detect any filaments due to sensitivity limitation and lack of enough short baselines. The flux densities of point sources in the GMRT map are compared with the flux densities from NRAO VLA Sky Survey (NVSS) map at 1.4 GHz and they matched within 10–15 per cent. The brightest filament seen in both the 325 and the 610 MHz GMRT maps is also seen as a $4\sigma$ feature in the NVSS map that has an rms of 0.7 mJy beam$^{-1}$.

Tian et al. (2010) overlaid the X-ray map with the 1.4 GHz SGPS contour map, which revealed that the X-ray emission extends beyond the radio shell towards the northern region (see fig. 1 of Tian et al. 2010). This is not expected since X-rays are found to be non-thermal (Tian et al. 2010; Abramowski et al. 2011; Bamba et al. 2012). The non-thermal X-ray and radio emission is expected to come from the synchrotron radiation from relativistic electrons accelerated at the shock. However, our 325 MHz GMRT maps clearly show radio emission to be present in this region also, eliminating this discrepancy.

The bright compact source G353.464−0.690 (Zoonematkermani et al. 1990) inside the remnant which is seen in the 1.4 GHz SGPS image is not seen in the GMRT map. This is because we have subtracted point sources during our analysis. The bright radio source J173028−344144 (Condon et al. 1998) seen towards the west of the SNR is an H II region. The extended structure seen further west is also likely to be an H II region since both of these are seen in the IRAS 60 $\mu$m map (Neugebauer et al. 1984) and the *WISE* 22 $\mu$m map (Wright et al. 2010).

The integrated flux density of the SNR at the 325 MHz is $1.84 \pm 0.15$ Jy. For a typical SNR spectral index of $\alpha \sim -0.5$ (Jones et al. 1998), the flux density of the SNR at 1420 MHz is expected to be 0.88 Jy. Tian et al. (2008) derived 1420 MHz flux density using combined Australia Telescope Compact Array and Parkes telescope data to be $2.2\pm0.9$ Jy. This value is likely to be an overestimation due to the contamination from thermal emission from nearby H II region. This discrepancy may also be due to the flux density estimation made by Tian et al. (2008) by taking one-half of the SNR (half towards low Galactic latitude) and extrapolating to the other half to estimate the complete flux density. However, our values match within $1.5\sigma$ with that of Tian et al. (2008). The change in flux density in the low-frequency end will change the shape of the spectral energy distribution (SED) and the parameters derived from multiwavelength models.

### 4.2 Central compact object

A bright compact object, XMMS J173203−344518, was discovered in the X-ray band near the centre of the SNR by Tian et al. (2010) from the *XMM* observations. The CCO was also seen in the *Suzaku* and the *Chandra* data (Halpern & Gotthelf 2010a). A marginal pulsation period of 1 s was found for the XMMS J173203−344518, which is between the periods of magnetars (2–12 s) and the CCOs (0.1–0.4 s) (Halpern & Gotthelf 2010a). However, Halpern & Gotthelf (2010b) failed to confirm this pulsation with the later *Chandra* observations. There is no evidence for a radio counterpart for this object (Tian et al. 2010). We did not detect radio emission at the CCO position in the GMRT observations at any frequencies. We provide deep limits on any possible radio counterpart of the CCO. The $3\sigma$ flux density upper limits at the CCO position are 727, 780 and 184 μJy at the 325, 610 and 1390 MHz, respectively, from our GMRT high-resolution maps.

### 4.3 Spectral index

The global radio spectral index of the SNR cannot be determined since the complete shell is not detected at the 610 MHz. We determined the spectral indices of four filaments of the SNR labelled 1–4 in the Fig. 1. The physical dimensions in angular units and flux densities at the 325 and 610 MHz of the filaments are listed in Table 3. The sizes of the filaments are less than 11 arcmin with less than 2 per cent missing flux at both the 610 and the 325 MHz observations. We have also accounted for the background contribution to the SNR flux density. However, these are statistical estimates, and the contribution of background flux density at the SNR position is uncertain.

The spectral index values are $-0.70 \pm 0.19$, $-1.11 \pm 0.22$, $-0.5 \pm 0.3$ and $-0.15 \pm 0.32$ for the filament 1, 2, 3 and 4 respectively. The spectral index values are broadly consistent with the non-thermal emission. The spectral index of the H II region is found to be $0.63 \pm 0.14$, which is consistent with thermal emission.

Here we note a steeper spectral index $-1.11 \pm 0.22$ for the filament 2. This steepening is consistent with synchrotron cooling that steepens the spectrum by a factor of $\Delta\alpha = 0.5$ from normal synchrotron spectral index. If this steepening is real, this could have important implications for the magnetic field in the SNR shell, and thus the VHE emission scenario (see Section 4.4). Our future observations with the upgraded GMRT with 200 MHz bandwidth and 2.5 times higher sensitivity compared to the existing GMRT will be very crucial here to determine the precise spectral indices with much improved error bars. The wide bandwidth of upgraded GMRT provides excellent *uv* coverage, thus more sensitivity to faint extended radio emission, which is crucial in accurately determining the spectral indices of the filaments.

### 4.4 Comparison with the VHE emission

Since the structure of the SNR is clearly detected in the 325 MHz radio map, the spatial correlation of the radio emission with that of the VHE emission can be compared. We compared the sites of synchrotron radio emission with the VHE emission measured with the HESS (Abramowski et al. 2011), as shown in Fig. 2. The spatial extent of the radio emission is similar to that of the VHE emission except for the region towards the west, where there is no radio emission though bright VHE emission is seen. It is likely that the radio emission in this region is sensitivity limited as this region has higher rms, due to the contribution from contamination from

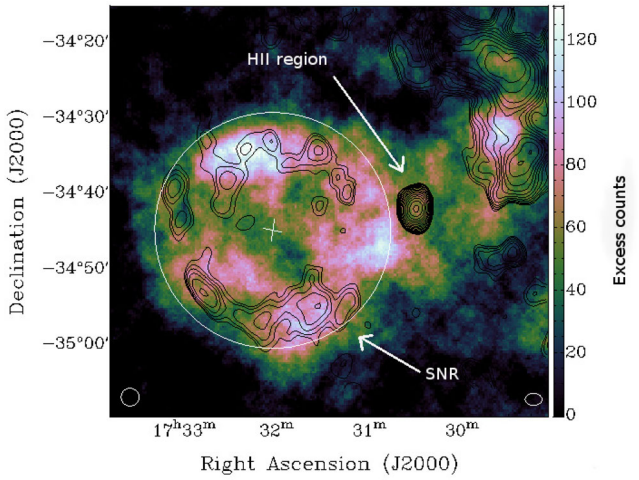


**Figure 2.** TeV $\gamma$-ray excess map (Abramowski et al. 2011) (resolution $144 \times 144$ arcsec$^2$; shown in the bottom left corner of the image) overlaid with GMRT 325 MHz map (resolution $135 \times 97$ arcsec$^2$; shown in the bottom right corner of the image) contours. The scale of the $\gamma$-ray excess map is excess counts per smoothing Gaussian width ($\sigma = 0.^\circ04$). The contours are $\pm\sqrt{2}^n \sigma$ mJy beam$^{-1}$ ($n = -2, 2, 3, 4, 5, 6$; $\sigma$=1.5 mJy beam$^{-1}$). The circle indicates the area enclosing SNR G353.6−0.7 centred at the CCO position (marked with a cross). The colour scheme used in the map is cubehelix (Green 2011)

nearby sources. The $3\sigma$ upper limit of flux density in this region at 325 MHz is 63 mJy, which is comparable to the flux densities of filaments 3 and 4 (see Table 3). The morphology of the SNR is shell-like in both radio and VHE emission, but the finer structure do not seem to be correlated. The bright filaments in radio (south-east filament and eastern filament, see Fig. 2) is faint in VHE map. The peak in VHE emission is from the north-east region, where the radio emission is faint (see Fig. 2).

The azimuthal variation in radio brightness can be either due to the gradient of ambient interstellar medium (ISM) density or due to the gradient of the magnetic field strength at the shock. An encounter of SNR G353.6−0.7 with a dense molecular cloud can create a density gradient in the ambient ISM, though, so far, there is no evidence for such an interaction. The $^{12}$CO spectra from the vicinity of SNR G353.6−0.7 obtained by Abramowski et al. (2011) does not show any kinematic features that account for a possible interaction of the SNR with a molecular cloud as reported in many interacting SNRs (e.g. Moriguchi et al. 2005; Castelletti et al. 2013). The $\gamma$-ray azimuthal profile of SNR G353.6−0.7 is roughly flat (Abramowski et al. 2011) except for the two $\gamma$-ray peaks towards the north-east and west, which is suggestive of a fairly uniform ambient ISM density (Abramowski et al. 2011). The shell structure of the SNR recovered in the 325 MHz GMRT map is fairly symmetrical. These three arguments suggest non-interaction of SNR G353.6−0.7 with a molecular cloud. Hence, it is reasonable to assume that the medium surrounding the SNR is of reasonably uniform density.

In such a case, the variation in radio brightness can be most likely due to the variation of magnetic field if the injection is isotropic (the efficiency of injection does not depend on the angle between shock normal and magnetic field). Radio brightness increases in the region of high magnetic field since synchrotron emissivity is proportional to $B^{3/2}$ for a particle distribution $N(E)$ scaling as $E^{-2}$. If the VHE emission is of leptonic origin, the electrons of energies $E \sim E_{\rm max}$ emit VHE $\gamma$-rays. These electrons experience ample radiative losses

in this region and the energy loss rate is proportional to $E^2B^2$. Thus, in the region of high magnetic field, the number of electrons emitting inverse Compton (IC) $\gamma$-rays deplete faster. This results in a low brightness of VHE emission where the radio brightness is still high (Petruk et al. 2009b), thus potentially explain the anticorrelation in the radio and $\gamma$-ray emission. This explanation is valid only in the case of synchrotron loss-limited acceleration scenario where $E_{\rm max} \propto B^{-1/2}$ (Reynolds 2008). In the case of age-limited acceleration scenario, $E_{\rm max} \propto B$ (Reynolds 2008) and the anticorrelation cannot be explained. However, the age of SNR G353.6−0.7 is not well known. The age estimates in the literature range from 2000 to 27 000 yr (Tian et al. 2008; Abramowski et al. 2011; Fukuda et al. 2014; Acero et al. 2015).

According to this model, we explain the anticorrelated emission of radio and VHE for SNR G353.6-0.7 in a leptonic scenario as follows: evidence of variation of magnetic field for SNR G353.6-0.7 comes from the analysis of spectral indices in Section 4.3. Here we see roughly a 0.5 steepening of the spectral index of filament 2 compared to the typical SNR spectral index of −0.5, consistent with synchrotron cooling, indicating higher magnetic field in this filament. Thus, the magnetic field strength is relatively high in the region of the south-east and eastern filaments, and hence it is bright in radio. Due to high synchrotron cooling, there are fewer IC electrons, and hence the VHE emission is faint here. The magnetic field strength is low towards the northern region of the SNR, and this results in less energy loss of electrons and bright IC emission. Towards the west, magnetic field strength is likely to be similar or less than that of the northern region, and the synchrotron emission is below the sensitivity limits where VHE emission is bright. One needs to measure local magnetic field using Zeeman splitting of OH maser spots (Brogan et al. 2000). Magnetic field can also be estimated from the rim-width of thin X-ray filaments by high-resolution X-ray observations (Parizot et al. 2006; Park et al. 2009). The roughly 0.5 steepening of the spectral index of filament 2 coincides with the region where the VHE emission is weakest, supporting the leptonic scenario in which the VHE production is suppressed due to synchrotron cooling in high magnetic field (Gabici & Aharonian 2016, and references therein). This provides a strong indication of leptonic origin of TeV $\gamma$-rays in SNR G353.6−0.7.

The presence of non-thermal X-ray emission further supports the leptonic origin of VHE emission. Non-thermal synchrotron X-ray emission implies the presence of TeV electrons that can easily produce IC $\gamma$-rays. The absence of any thermal X-ray emission further rules out hadronic origin of VHE emission as thermal X-ray emission is proportional to the square of the gas density, and hadronic processes are likely to dominate in high-density regions (Gabici & Aharonian 2016). However, the hadronic scenario is still possible if the SNR shock has not been able to heat the gas to high temperature if the gas is clumpy, then the dense clump can produce TeV $\gamma$-rays via hadronic process (Gabici & Aharonian 2014).

This radio-VHE anticorrelation trend is not seen in any of the other four SNRs in the VHE shell class. In fact, correlated emission of synchrotron radio and IC $\gamma$-ray emission is seen in the bilateral SNR 1006 (Petruk et al. 2009a; Acero et al. 2010). This correlated emission is explained by the variation of maximum energy of electrons over the SNR to compensate for magnetic field variation (Petruk et al. 2009b). This can also happen if the dependence of injection and the electron maximum energy on the obliquity angle (angle between magnetic field and the normal to the shock) is strong enough to dominate the magnetic field variations (Petruk et al. 2009b).

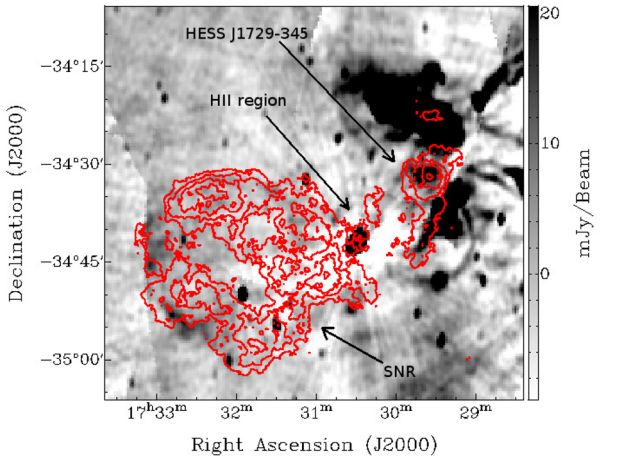


**Figure 3.** MOST map (Green et al. 1999) of the field containing G353.6−0.7 at 843 MHz overlaid with HESS contours with levels 6, 8, 10, 12$\sigma$ ($\sigma$ = 10 counts). TeV map (Abramowski et al. 2011)

Visual inspection of Fig. 2 suggests the VHE emission to be slightly beyond the radio shell. However, the extent of radio emission could be due to sensitivity limitation. An upgraded GMRT observation with 200 MHz bandwidth will provide 2.5 times the sensitivity and excellent *uv* coverage. Thus, it will be more sensitive to the fainter extended features and will be tracing the true extent of the radio emission.

### 4.5 Radio counterpart of nearby TeV source HESS J1729−345

There is another TeV source, HESS J1729−345, at position $\alpha_{\rm J2000}$ = $17^{\rm h}29^{\rm m}35^{\rm s}$, $\delta_{\rm J2000}$ = $-34^\circ32'22''$, ∼ 30 arcmin away from the centre of HESS J1731−347 with no identified counterpart in other wavebands (Abramowski et al. 2011). This source is located near an H II region (G353.381−0.114) and a molecular gas clump in spatial projection (Abramowski et al. 2011). Abramowski et al. (2011) estimate near and far kinematic distances towards this molecular clump at ∼ 6 and ∼ 10 kpc, respectively, from $^{12}$CO molecular line observations. If HESS J1729−345 is associated with HESS J1731−347, which is only 3.2 kpc away, this molecular clump cannot be in the vicinity of HESS J1729−345 (Abramowski et al. 2011).

The TeV emission from HESS J1729−345 has been explained by Cui, Pühlhofer & Santangelo (2016) with a hadronic scenario, due to the interaction of the SNR with the surrounding molecular material (as observed from $^{12}$CO emission), via proton–proton collision. In that case, $\gamma$-ray photons would be produced by proton–proton interaction, and synchrotron radio emission is not expected unless the secondary leptons produced by the decay of charged pions radiate significantly. However, in order for this emission to be important, it requires rather high densities and magnetic fields.

HESS J1729−345 was observed in both the 325 and 1390 MHz bands. Radio emission is not seen in spatial coincidence with HESS J1729−345 in the 1390 MHz GMRT map. In the 325 MHz map, the diffuse radio emission towards the west overlaps the region of HESS J1729−345 (see Fig. 2). The morphology of the emission does not seem to be corresponding to HESS J1729−345, which is ∼ 7 arcmin Gaussian structure. However, a possible radio counterpart of HESS J1729−345 is seen in the 843 MHz MOST (see Fig. 3) and the 1.4 GHz SGPS maps. The non-detection in the 1390 MHz GMRT map can be due to missing flux. Our GMRT map at 1390 MHz is

sensitive to angular scales up to 4 arcmin. Thus significant flux will be missing while imaging a 7 arcmin structure. We obtain a spectral index of $3.0 \pm 0.2$, from the 843 MHz MOST map and the 1.4 GHz SGPS map, which is consistent with thermal emission. Thus, the radio emission from this possible counterpart is not synchrotron in nature. We note that Cui et al. (2016) explained VHE emission from HESS J1729−345 in a hadronic scenario. The positive spectral index of the possible radio counterpart supports this explanation.

## 5 SUMMARY AND CONCLUSIONS

We carried out the GMRT observations of HESS J1731−347 also known as SNR G353.6−0.7 in the 325, 610 and 1390 MHz band. We also observed a nearby source, HESS J1729−345 with the GMRT in the 325 and 1390 MHz frequency bands to look for possible radio counterparts. Our conclusions are as follows.

(i) We detect the low-frequency radio morphology of SNR G353.6−0.7 with the GMRT at the 325 and 610 MHz frequencies. The shell structure of the SNR with diffuse filaments is revealed in the 325 MHz map, and SNR is partially seen in the 610 MHz map.

(ii) The integrated flux density of the SNR at the 325 MHz frequency is 1.84±0.15 Jy. Assuming a typical spectral index of −0.5 for SNRs, we derive the integrated flux density at the 1.4 GHz as 0.88 Jy. We note that this value is $1.5\sigma$ lower than the previously reported flux density 2.2±0.9 Jy at 1.4 GHz (Tian et al. 2008). The change in radio flux density changes the SED slightly.

(iii) The spectral indices of the different filaments are estimated from the 325 and 610 MHz GMRT maps. The values of spectral indices vary from −1.11 to −0.15 and are consistent with the non-thermal radio emission.

(iv) We compare the radio brightness profile with the VHE emission. It is particularly striking that the peak in $\gamma$-ray emission comes from the filament that is faintest in the radio, and the brightest filaments in the radio correspond to faint emission in $\gamma$-rays. The faintest filament in $\gamma$-rays also shows a steep spectral index of $-1.11 \pm 0.22$. This may be due to the effect of non-uniform magnetic field strength, which is suggestive from the possible evidence of synchrotron cooling in that region of the SNR. In this framework, the anticorrelated emission can be explained if the VHE emission is of leptonic origin for an isotropic injection. This kind of an anticorrelated emission is reported for the first time in VHE shell SNRs.

(v) The visual extent of the VHE emission appears to be slightly beyond the radio shell. However, our radio observations are most likely sensitivity-limited. Future radio observations with better sensitivity will probe the true extent of the SNR and the upgraded GMRT observations with 2.5 times higher sensitivity and an order of magnitude larger bandwidth will prove to be useful for this.

(vi) We also report a possible radio counterpart of HESS J1729−345 from the 843 MHz MOST map and the 1.4 GHz SGPS map. The radio emission is thermal and it supports the hadronic origin of $\gamma$-rays from HESS J1729 −345.

## ACKNOWLEDGEMENTS

We thank the anonymous referee for constructive inputs. We acknowledge Nissim Kanekar and Aritra Basu for their support at various stages of this work. PC acknowledges support from the Department of Science and Technology via SwaranaJayanti Fellowship award (file no. DST/SJF/PSA-01/2014-15). We thank the staff of the GMRT that made these observations possible. GMRT is run by the National Centre for Radio Astrophysics of the Tata Institute of Fundamental Research.

## REFERENCES

Acero F., Pühlhofer G., Klochkov D., Komin N., Gallant Y., Horns D., Santangelo A. H., H. E. S. S. Collaboration, 2009, preprint (arXiv:0907.0642)
Acero F. et al., 2010, A&A, 516, A62
Acero F., Lemoine-Goumard M., Renaud M., Ballet J., Hewitt J. W., Rousseau R., Tanaka T., 2015, A&A, 580, A74
Aharonian F. A. et al., 2004, Nature, 432, 75
Aharonian F. et al., 2007, ApJ, 661, 236
Aharonian F. et al., 2008, A&A, 477, 353
Aharonian F. et al., 2009, ApJ, 692, 1500
Bamba A. et al., 2012, ApJ, 756, 149
Basu A., Mitra D., Wadadekar Y., Ishwara-Chandra C. H., 2012, MNRAS, 419, 1136
Blandford R., Eichler D., 1987, Phys. Rep., 154, 1
Blasi P., 2013, A&AR, 21, 70
Brogan C. L., Frail D. A., Goss W. M., Troland T. H., 2000, ApJ, 537, 875
Castelletti G., Supan L., Dubner G., Joshi B. C., Surnis M. P., 2013, A&A, 557, L15
Condon J. J., Cotton W. D., Greisen E. W., Yin Q. F., Perley R. A., Taylor G. B., Broderick J. J., 1998, AJ, 115, 1693
Cui Y., Pühlhofer G., Santangelo A., 2016, A&A, 591, A68
Degrange B., Fontaine G., 2015, C. R. Phys., 16, 587
Fukuda T., Yoshiike S., Sano H., Torii K., Yamamoto H., Acero F., Fukui Y., 2014, ApJ, 788, 94
Gabici S., Aharonian F. A., 2014, MNRAS, 445, L70
Gabici S., Aharonian F., 2016, EPJ Web Conf., 121, 04001
Green D. A., 2011, Bull. Astron. Soc. India, 39, 289
Green A. J., Cram L. E., Large M. I., Ye T., 1999, ApJS, 122, 207
Greisen E. W., 2003, in Heck A., ed., Astrophysics and Space Science Library, Vol. 285, Information Handling in Astronomy - Historical Vistas. Kluwer Academic Publishers, Dordrecht, p. 109
H. E. S. S. Collaboration et al., 2011, A&A, 531, A81
H. E. S. S. Collaboration et al., 2016a, preprint (arXiv:1609.08671)
H. E. S. S. Collaboration et al., 2016b, preprint (arXiv:1611.01863)
H. E. S. S. Collaboration et al., 2016c, preprint (arXiv:1601.04461)
Halpern J. P., Gotthelf E. V., 2010a, ApJ, 710, 941
Halpern J. P., Gotthelf E. V., 2010b, ApJ, 725, 1384
Haslam C. G. T., Salter C. J., Stoffel H., Wilson W. E., 1982, A&AS, 47, 1
Haverkorn M., Gaensler B. M., McClure-Griffiths N. M., Dickey J. M., Green A. J., 2006, ApJS, 167, 230
Jones T. W. et al., 1998, PASP, 110, 125
Landecker T. L., Wielebinski R., 1970, Aust. J. Phys. Astrophys. Suppl., 16, 1
Marcote B., Ribó M., Paredes J. M., Ishwara-Chandra C. H., 2015, MNRAS, 451, 59
Moriguchi Y., Tamura K., Tawara Y., Sasago H., Yamaoka K., Onishi T., Fukui Y., 2005, ApJ, 631, 947
Neugebauer G. et al., 1984, ApJ, 278, L1
Parizot E., Marcowith A., Ballet J., Gallant Y. A., 2006, A&A, 453, 387
Park S., Kargaltsev O., Pavlov G. G., Mori K., Slane P. O., Hughes J. P., Burrows D. N., Garmire G. P., 2009, ApJ, 695, 431
Petruk O., Dubner G., Castelletti G. et al., 2009a, MNRAS, 393, 1034
Petruk O., Beshley V., Bocchino F., Orlando S., 2009b, MNRAS, 395, 1467
Reynolds S. P., 2008, ARA&A, 46, 89
Roger R. S., Costain C. H., Landecker T. L., Swerdlyk C. M., 1999, A&AS, 137, 7
Sirothia S. K., 2009, MNRAS, 398, 853

Swarup G., Ananthakrishnan S., Kapahi V. K., Rao A. P., Subrahmanya C. R., Kulkarni V. K., 1991, Curr. Sci., 60, 95
Tian W. W., Leahy D. A., Haverkorn M., Jiang B., 2008, ApJ, 679, L85
Tian W. W., Li Z., Leahy D. A., Yang J., Yang X. J., Yamazaki R., Lu D., 2010, ApJ, 712, 790
Wright E. L. et al., 2010, AJ, 140, 1868
Yang R.-Z., Zhang X., Yuan Q., Liu S., 2014, A&A, 567, A23
Zoonematkermani S., Helfand D. J., Becker R. H., White R. L., Perley R. A., 1990, ApJS, 74, 181

This paper has been typeset from a TEX/LATEX file prepared by the author.